Near Surface Geophysics, 2014, **12**, 151-163 doi:10.3997/1873-0604.2013017

Real-time electrical monitoring of reagent delivery during a subsurface amendment experiment

Dale F. Rucker[1*], Nigel Crook[2], Jeffrey Winterton[3], Michael McNeill[2], Chris A. Baldyga[1], Gillian Noonan[1] and James B. Fink[1]

[1] *hydroGEOPHYSICS, Inc., 2302 North Forbes Boulevard, Tucson, AZ 85745, USA*
[2] *hydroGEOPHYSICS, Inc., 1806 Terminal Drive, Richland, WA 99354*
[3] *AngloGold Ashanti, Denver, CO*

Received May 2012, accepted April 2013

ABSTRACT

An electrical resistivity monitoring survey was conducted on a mine heap to track reagent movement during high-pressure injections. The injections were designed to increase the dissolution of metallic gold from low-grade ore and enhance recovery after surface leaching had ceased. The main objective of the geoelectrical monitoring was to observe the effectiveness of the injection technique and provide feedback to optimize injection parameters in real time. Real-time assessment was achieved by monitoring the raw output current and transfer resistance on a network of borehole electrodes installed around the injection well. It was demonstrated that the output current increased significantly on particular borehole electrodes after commencement of reagent injection, when the wetting front arrived at the electrodes. When injection ceased, the electrical current returned to the initial baseline current values. The timing and distribution of the electrodes demonstrating this behaviour varied with injection depth. The internal structure of the heap was likely a controlling factor in reagent movement. Resistance, converted to apparent resistivity, was also shown to change significantly in the region near the injection. Verification of the real-time assessment was conducted with post-injection time-lapse 3D tomographic inversion. While inverse modelling provides a truer 3D representation of reagent injection, the cost was shown to be a time-lag of 3.5 days to complete the modelling. The simplicity of monitoring the raw current output and voltage can make this a powerful tool for real-time tracking of fluid movement in the subsurface.

INTRODUCTION

In situ reagent delivery is a common means to amend soil and groundwater chemistry for environmental and agricultural applications or to increase the efficiency of resource extraction in the oil, gas and mineral industries. The delivery mechanism may include a surface application, such as surface leaching (Navarro and Martínez 2010) or soil flushing (Lwambiyi *et al.* 2009; Svab *et al.* 2009; Lee, Kim and Kim 2011). Alternatively, reagents may be applied directly to a zone of interest through the use of injection wells. A well application can administer the reagents under a natural gradient. For example, Ha *et al.* (2011) conducted a natural gradient drift test to assess the *in situ* aerobic metabolism of trichloroethylene, or as active (i.e., pressurized) injections to transport the reagent more quickly through the groundwater.

Regardless of the delivery mechanism, understanding the fate of the reagent and its intended target is difficult without the inclusion of geophysically-based imaging techniques. Geophysical methods typically have an advantage in obtaining spatial information, as they can sense changes far from the sampling location by measuring some degree of energy transport through the entire region of interest. Unfortunately, the methods tend to be hampered temporally because geophysical data can be slow to acquire and analyse. The electrical resistivity method is not a real-time monitoring tool, although several authors have described the technique as obtaining 'near' real-time images of the subsurface (Rucker 2009; Wilkinson *et al.* 2010; Rucker, Fink and Loke 2011). A finite amount of time is required to acquire a complete set of measurements (Robert *et al*. 2012), even with modern equipment incorporating multiple channels and multi-core cables. Additionally, measured data include associated noise (from ground coupling, instrument, etc.) and it is important to remove such low-quality data prior to inverse modelling (LaBrecque *et al*. 1996), requiring additional time to conduct. Autonomous resistivity systems, such as those described in LaBrecque *et al.* (2004), Wilkinson *et al.* (2010) and Calendine *et al.* (2011), are helping to reduce the total time from acquisition to interpretation.

* drucker@hgiworld.com

There are aspects to the electrical resistivity method, other than generating inverse modelled images, which can truly be evaluated in real time. Mechanistically, the method requires an electrical current (I) to be transmitted into the ground across a pair of electrodes and the voltage (V) to be measured across a different pair of electrodes, prior to any processing and inverse modelling. These two measurements can be viewed in real time as they are acquired and the information used as a high-level tool to discriminate changes in the subsurface. In this work, we demonstrate the use of raw current and voltage data (converted to transfer resistance and then apparent resistivity) for evaluating an amendment process in a mine heap of low-grade ore. The amendment process includes injecting dilute sodium cyanide solution under a forced gradient to enhance the transport of dissolved gold. The injection procedure is conducted after the primary leaching cycle to promote flushing of reagent trapped in lower permeable pore spaces, break preferential flow paths that may have established within the heap (Rucker *et al.* 2009a) and increase recovery of ore beneath side slopes that are traditionally under leached. The electrical data allow optimization of the process by providing information about the movement of the reagent in addition to providing a level of safety, such that the high rate of injection does not compromise the integrity of the heap's slope. Lastly, we compare the initial interpretations gained from the real-time assessment to the more commonly applied inverse modelling approach, or electrical resistivity tomography and show that the former matches the latter with respect to directionality of the reagent's migration and extent of coverage.

RESITIVITY ACQUISITON

Monitoring electrical current

Consider a point electrode, buried in a homogeneous earth of resistivity, ρ. From Telford, Geldart and Sheriff (1990), the strength of the electrical field, E, for a given current passed between the buried source electrode and another point electrode placed at distance is:

$$E = -\frac{dV}{dr} = \frac{\rho I}{4\pi r^2} \tag{1}$$

where r is the distance of the field from the buried source electrode. Now assume that at some future time during the injection of a reagent into the subsurface, the fluid front encroaches on the source electrode. The resistivity of the saturated earth is ρ_1 (where $\rho_1 << \rho$) at a distance of r_1 or greater and the resistivity of the earth immediately around the electrode remains dry with a value of ρ (Fig. 1). Integrating equation (1), using the prescribed boundary conditions, we obtain:

$$V = \frac{I}{4\pi}\left(\frac{\rho}{r} + \frac{(\rho_1 - \rho)}{r_1}\right),\ r \le r_1$$
$$V = \frac{\rho_1 I}{4\pi r},\ r > r_1 \tag{2}$$

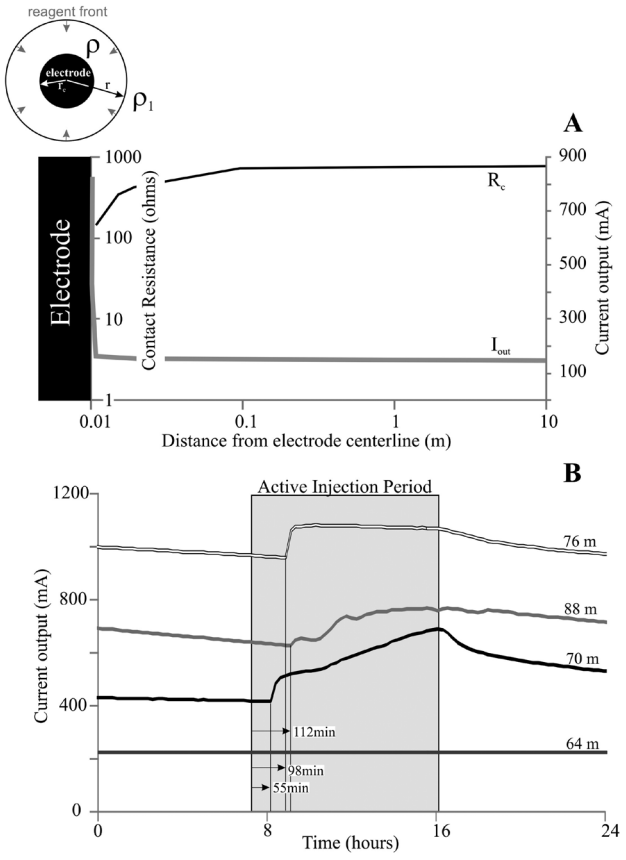

FIGURE 1

Contact resistance and current output for an electrode embedded in the earth experiencing reagent injection. a) Ideal model for a shrinking sphere, modelled from equation (3) with ρ = 100 ohm-m, ρ_1 = 10 ohm-m and r = 0.01 m. b) Measured electrical current during an actual injection with borehole electrodes at depths of 64, 70, 76 and 88 m below ground surface.

Using the same logic in Lile, Morris and Rønning (1997) with Ohm's law allowing the conversion of voltage to a contact resistance (R_c), an electrode in contact with the earth assuming unity current will exhibit the following behaviour:

$$R_c = \frac{1}{4\pi}\left(\frac{\rho}{r} + \frac{(\rho_1 - \rho)}{r_1}\right) \tag{3}$$

Considering the electrode's radius as r_e, the resistance at the electrode-earth interface will be that of equation (3) by substituting r_e for r. In our implementation of electrical resistivity acquisition with the 180-channel Geotection system (hydroGEOPHYSICS, Inc. Tucson, AZ), we hold the driving voltage constant across the pair of transmission electrodes at 120 V. The specific quantity of output current, I_{out}, is inversely related to the contact resistance, from Ohm's law. Continuing with the advancing reagent example, as the fluid moves closer to the electrode and $r_1 \rightarrow r_e$, one would expect the contact resistance to drop and current output to increase. Figure 1(a) displays a model of these

phenomena using values of ρ = 100 ohm-m, ρ_1 = 10 ohm-m and an electrode radius of 0.01 m. The example demonstrates that the output current does increase substantially but only when the fluid front is less than 0.01 m from the electrode. In this case, as the fluid front moves from a distance of 1 to 0.02 m from the electrode, the output current increases by only 10%. However, at distances of 0.01 and 0.001 m from the electrode, there is an approximate 2-fold and 5-fold increase in output current, respectively. The specific degree of change in post-arrival current is dependent on the contrast between the wet and dry soil.

The model presented above is a simplified representation of the electrode system and others have modelled contact resistance in more detail. Rücker and Günther (2011) used a complete electrode model incorporating a contact impedance between the electrode and earth, in addition to a condition for the current flow through the electrode surface, to more realistically model current and voltage in the vicinity of the electrode. In our work, we do not believe this level of detail is necessary. We are not interested in obtaining specific electrode or earth properties. Instead, we are only using the point at which the output current increases as a monitoring tool to time fluid front arrivals at the electrode. By knowing when the current increases substantially, the electrode can benchmark the location of the fluid front. If a sufficient number of electrodes exist, then a detailed picture emerges regarding the reagent distribution during injection.

To demonstrate the concept of increasing electrical current from an empirical point of view, field data are plotted from an injection experiment (Fig. 1b). The Methods section provides more detail regarding the experiment. For the data plotted in Fig. 1(b), an electrode array was installed in a borehole located 12.2 m from the injection well with electrode spacing of ~6 m, extending from the surface to 94 m below ground surface (bgs). The electrical resistivity monitoring system cycled through the electrode combinations every 14 minutes using a pole-pole configuration; the remote (infinite) electrode necessary to complete the circuit was placed approximately 700 m away from the injection. Prior to any reagent injection the output current for each electrode was constant and Fig. 1(b) displays the output for four of the electrodes in the borehole. The injection was initiated at 7:15 am at a depth of 64 m (bgs) and lasted 525 minutes. Three of the electrodes within the borehole registered an arrival, as indicated by the current increase through time. Shortly after the injection commenced, the electrode at a depth of 70 m (bgs) registered an arrival after 55 minutes of injection commencement. The next series of arrivals occurred at the electrodes at depths of 76 and 88 m (bgs), after 98 and 112 minutes of injection commencement, respectively. After the injection ceased, the current began to drop as the reagent drained away from the electrode's vicinity. In contrast, the electrode at the same depth as the injection, at 64 m (bgs), registered no change during the course of delivery.

Monitoring voltage potential

In a slightly different setup than presented above, consider a steel cased well used to inject a reagent into the subsurface. The injection well can also be safely utilized as a long electrode to pass current as part of the electrical monitoring system (Rucker *et al.* 2010). The voltage potential at a depth of z in a homogeneous half-space of resistivity ρ is (Johnston, Trofimenkoff and Hasslett 1987; Warrick and Rojano 1999):

$$V = \frac{\rho I}{4\pi b} \ln \left[\frac{z+b+\sqrt{r^2+(z+b)^2}}{z-b+\sqrt{r^2+(z-b)^2}} \right] \quad (4)$$

where b is the length of the injection well and r is the lateral distance between the well and the location of the voltage measurement. The derivation of equation (4) assumes a finite line

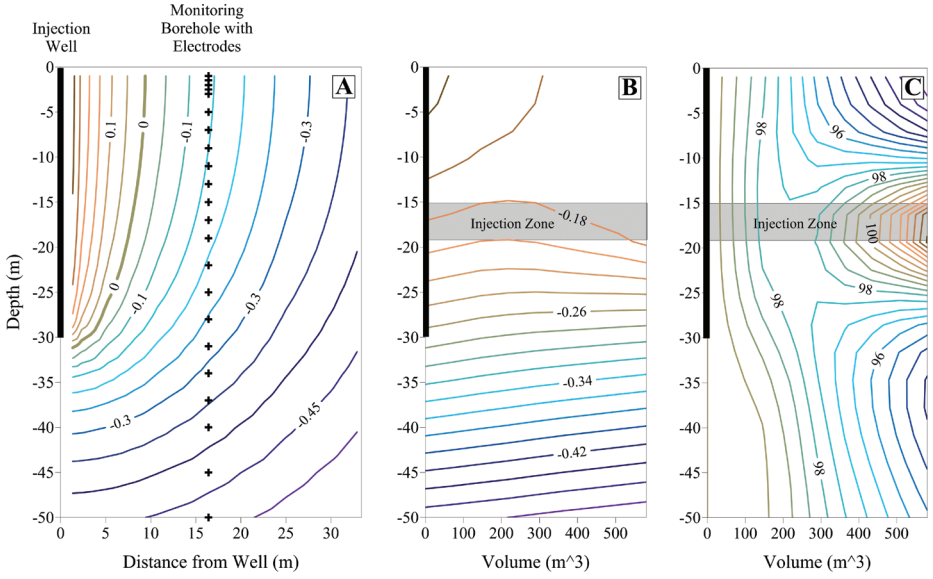

FIGURE 2
Voltage distribution during injection. a) Analytical model for a homogeneous half-space with a resistivity of 100 ohm-m, presented as log-transformed voltage. b) Log-transformed voltage during injection as a function of injected volume, measured 16.4 m away from the injection well. The injection was modelled as cylinder with a height of 4 m. c) Apparent resistivity during injection as a function of injected volume, measured 16.4 m away from the injection well.

source with the current uniformly distributed along its length and infinitesimal resistivity. The resistivity can be obtained by simply rearranging equation (4):

$$\rho = \frac{4\pi bR}{\ln\left[\dfrac{z+b+\sqrt{r^2+(z+b)^2}}{z-b+\sqrt{r^2+(z-b)^2}}\right]} \quad (5)$$

where R is the transfer resistance, V/I. If equation (5) is used to convert measured field resistance data from electrodes either buried in the subsurface or on the surface, it is considered an apparent resistivity.

Figure 2(a) displays the voltage distribution for the case of a homogeneous half-space of 100 ohm-m, an injection well of 30 m length and an input current of 1 A; voltage is presented as log-transformed. Note, in proximity of the injection the equipotential lines are near vertical. As $r \rightarrow \infty$, the influence of the injection well is diminished and the distribution of the equipotential lines begins to converge to that of the typical point electrode source located at the surface, with a difference of less than 0.5% when $r/b \approx 10$.

Monitoring the change in voltage during an active injection can be conducted on a borehole electrode array at some distance away from the injection well. To demonstrate, a series of forward models were run using an expanding cylinder to simulate the ideal geometry for a reagent injection. The height of the cylinder remained constant at 4 m, with the top located at 15 m (bgs) and a resistivity of 1 ohm-m. For borehole electrodes located 16.4 m from the injection well, the voltage as a function of cylinder (or injection) volume is displayed in Fig. 2(b) for seven models using RES3DMODx64 (Geotomo Software, Malaysia). The figure is similar to the time series presentation of data in Pidlisecky, Cockett and Knight (2012). The figure displays smoothly varying voltage values that either decrease slightly above and below the injection zone or increase in the injection zone. The changes are subtle and it is difficult to interpret any details of the injection. If instead, we transformed the data to apparent resistivity using equation (5), the resulting contoured values reveal more detail with regards to the evolution of the equipotential line distribution (Fig. 2c). The injection zone now is readily seen as high-apparent resistivity values as the injection approaches and passes the position of the borehole array (equivalent to an injection volume of 412 m^3).

The advantage of using the apparent resistivity is that, like electrical current, the data can be viewed in real time as they are collected. The data of Fig. 2(c) is a simple transformation and plotting routine, which can reveal information about the subsurface for initial assessment. However, it is not a substitute for obtaining spatial properties, such as the true electrical resistivity, which are specifically related to the water content, ionic strength, or porosity.

Inverse modelling

Once all of the voltage and current measurements have been acquired on the electrode pairs of interest, the data can be inverse modelled to obtain an estimate of the true distribution of the subsurface resistivity. In the procedure, the resistivity of the subsurface is changed iteratively from an initial starting condition, usually homogeneous for 3D models, until the calculated apparent resistivity of the model closely matches that of the measured apparent resistivity in a least squares sense. How the model is updated depends on the specific formulation of the objective function and many have used spatial weighting matrices or roughness filters (Loke, Acworth and Dahlin 2003) to dampen noisy measurements or adjacent model cells and temporal dampening factors to minimize changes across time (Kim *et al.* 2009; Loke, Dahlin and Rucker 2013). There are many discussions of generalized and resistivity-specific inversion procedures in the literature and the reader is directed to Farquharson (2008), deGroot-Hedlin and Constable (1990), Loke and Barker (1996), Farquharson and Oldenburg (1998) and Constable, Parker and Constable (1987) for more information.

Unless a supercomputer is available (e.g., Johnson *et al.* 2010), it is likely that the time to complete the inverse modelling for a single snapshot is longer than the time to acquire the next snapshot. With this time difference between data acquisition and model production, the ability to understand the subsurface from resistivity in real time diminishes. Inverse modelling, therefore, is typically conducted after demobilization to ensure that noisy data are removed and inverse model parameters tested.

Finally, when evaluating the results of an inverse model, several qualitative and quantitative indicators can be used to ensure that the results match hydrological or geological expectations that were formed during the conceptual model phase of the project. From a qualitative point of view, the coherency of targets through image appraisal is important. We use coherency in this context to

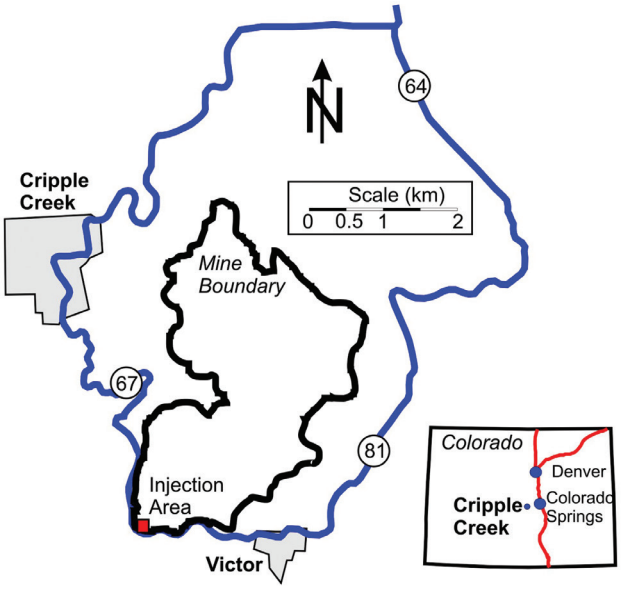

FIGURE 3
Location map of the Cripple Creek and Victor gold mine, central Colorado, showing the injection area within the mine's boundary.

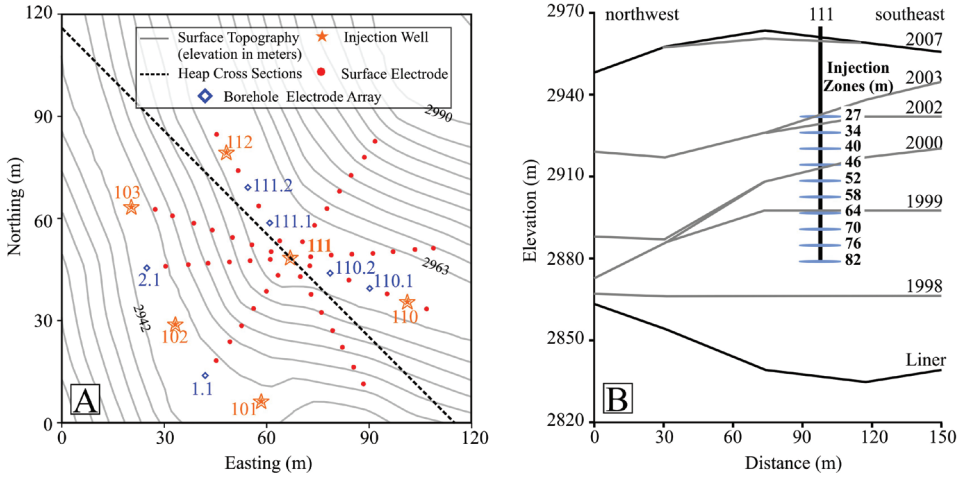

FIGURE 4
Layout of reagent delivery. a) Topographic map with injection wells (stars), surface electrodes (dots) and borehole electrode arrays (diamonds). b) Cross-section through the heap, as defined by the location on the topographic map. The cross-section shows variability in the heap topography by year. Also shown are the depths of injection zones from well 111.

describe how well the targets conform a smooth model, free of small-scale variabilities that are unrealistic with the technique. Quantitatively, most inversion codes will provide an estimate of the modelled data error relative to the measured data as a root mean square difference, with the objective of the inversion to minimize the difference between the two data sets.

Other quantitative indicators have included the model resolution matrix, sensitivity, or a depth of investigation (DOI) index. Alumbaugh and Newman (2000) used the model resolution to understand the effects of key assumptions from electromagnetic inversion models. The model resolution is a matrix that is computed from the Jacobian and other model constraints and describes how well the inversion model resolves the subsurface (Day-Lewis, Singha and Binley 2005). R may be viewed as a filter that blurs the true values of the subsurface resistivities (Stummer, Maurer and Green 2004). Nguyen *et al*. (2009) used data error-weighted cumulative sensitivity to show how specific areas of the imaging region are 'covered' by the data, by analogy to ray-based tomography. Robert *et al*. (2012) used a relative sensitivity matrix to gain more insight into the reliability of inversion results. Oldenburg and Li (1999) presented a method to measure the DOI by quantifying how much each region of the resistivity image changed by analysing the difference in two or more inversion results with different model constraints (Freidel 2003). In our work (e.g., Rucker 2012), we have primarily focused on the model resolution to investigate the consequence of typical decisions made for conducting resistivity surveys to resolve a target, including model parameters (inverse model cell size) and acquisition parameters (electrode density and array type).

METHODS

Setting

The reagent amendment occurred at the Cripple Creek and Victor gold mine, located in central Colorado (Fig. 3). Gold is produced from a valley fill leach pad, stacked from crushed ore mined from an open pit operation (Seal, Rucker and Winterton 2012). After stacking, an aqueous solution of sodium cyanide is applied at the surface, which percolates through the rock to preferentially dissolve the gold. The leach pad is underlain by an impermeable (and electrically insulating) liner to collect the gold-laden pregnant solution, which is pumped to the processing plant to extract and refine the gold for market. The barren solution is then recirculated back to the top of the leach pad to repeat the cycle. Due to the height of the pad, in excess of 180 m in places, it can take up to six months for the solution to complete this cycle.

The leach pad was constructed over several decades by end dumping ore from large dump trucks. The ore was stacked in a series of lifts, each upwards of 30 m in height. As a result of the dumping the topography is highly variable and steep in many areas. Figure 4(a) displays the study area near the reagent injection, with topography varying up to 72 m across the study site. A cross-section through the heap (Fig. 4b) reveals the position of the heap's surface through time, with the specific year of the surface located to the right. The liner dips towards the southwest, out of plane. Early in the heap's construction, the material was dumped fairly uniformly in thick sequences above the liner. At later times, the dumping created steep inclines towards the west, all of which may contribute to how the leaching solution moves downward through the pile. Rucker *et al.* (2009a) identified the heap structure as a component affecting moisture movement within heaps.

Reagent injection

Injection wells were installed in the heap to help enhance recovery of the gold. The injection wells were especially useful for regions deep within the leach pad, where changes made to the application of surface irrigation had no significant influence on flow patterns and geochemical conditions nearer the liner. The injection wells were located along benches for easy access, approximately 37 m apart and drilled to depths to within 30 m of the liner. Our study of reagent delivery was focused on injection well 111 (Fig. 4a).

Sodium cyanide solution was injected through a high-capacity pumping skid in a series of packed zones, starting at the bot-

tom of the well (82 m bgs) and progressing upwards at 6 m intervals until a safe distance from the surface was reached. Figure 4(b) displays the position of each injection zone relative to the heap construction. Typical injection scenarios included four hours of pumping at 3000 L/min. However, some zones were injected for eight hours to test the effect of injection time on recovery, or at lower pressures to gain an appreciation for the effectiveness of the highly pressurized injections. A total of 10 zones were injected over a period of eight days.

Geophysical survey design

To monitor reagent movement from the injection well, a radial design of surface electrodes was installed centrally around well 111 (Fig. 4a). The eight radials contained a total of 48 stainless steel electrodes. The choice of a radial arrangement over a regular grid arrangement of electrodes was twofold. Firstly, the radial design allowed for the use of cables with regular electrode take-out intervals. The cables were already in our inventory and were more cost effective than individually wiring each electrode within a grid. Secondly, the spacing between electrodes was approximately 6 m along each radial, whereas a grid array would have necessitated 12 m spacing in order to satisfy the 48 electrodes over a 72 m by 72 m grid. One potential disadvantage to the radial arrangement, however, could be in the resolution of the results of the inverse model on the outer edges of the domain where electrodes were absent. For example, Rucker *et al*. (2009a) showed artefacts in inverse modelling results at the domain edge for a radial arrangement of electrodes. Furthermore, several have used the grid arrangement to monitor the movement of plumes in the subsurface with great success (Doetsch *et al*. 2012). What is missing from the literature is a full analysis of which arrangement of electrodes is superior for each particular problem. Such an analysis is beyond the scope of this work.

In addition to the surface electrodes, six borehole electrode arrays were installed on the benches between the injection wells. On average 15 stainless steel electrodes were placed in each borehole array, varying from 14–17, with a base electrode separation of 6 m. An exception was made at the ends of the array, where electrode separation was 3 m. The total length of the borehole arrays varied between 55–95 m. Installation occurred by dangling the electrodes in the open hole and backfilling with moist cuttings material. A few borehole electrodes did not make good contact with the surrounding formation due to bridging of material above it during backfilling. Lastly, six of the nearby steel-cased injection wells were utilized as long electrodes, to pass current and measure voltage during injection (Rucker *et al*. 2010).

All of the electrodes were wired back to a central location for connection with a 180-channel electrical resistivity monitoring system. The electrical resistivity system was capable of connecting and recording 180 electrodes simultaneously, using the pole-pole array. If desired, the pole-pole data could be converted to any other array type to generate an image with superior resolution (e.g., Rucker 2012). For the 150 electrodes used to monitor injection well 111, a complete sweep of measurements including reciprocals, where each electrode received a turn at passing current while all others recorded voltage, was completed in 14 minutes. Over the eight days of injections, 780 snapshots were produced. Table 1 lists the pertinent acquisition parameters of the survey and of the Geotection system. Figure 5 highlights some of the raw data, including transfer resistance and reciprocal errors. Specifically, Fig. 5(a) shows the transfer resistance versus geometric factor for two times during the last day of monitoring. Figure 5(b) highlights the time series transfer resistance of two electrodes on channels 8 and 9 (within borehole 102), with each electrode acting as either a transmitting electrode or receiving electrode. There is a clear separation between the two series, which is quite common to all reciprocal pairs. Figure 5(c) shows the complete set of reciprocal errors for one snapshot, just before injections started on the last day of monitoring. The reciprocal errors have an average of –0.02%. Overall, the transfer resistance data are free of excessive noise.

RESULTS

The first reagent injection was conducted at a depth of 82 m (bgs), starting around noon on the first day (Day 0 indicates the first day in all subsequent graphs). The electrical resistivity

TABLE 1
Resistivity acquisition parameters during injection monitoring.

Acquisition Parameter	Value	Acquisition Parameter	Value
Array Type	Pole-pole	Number of data values per snapshot, including long electrodes and reciprocals	17952
Total Electrodes / Channels	150	Number of data values per snapshot used in the inverse modeling (excludes reciprocals)	6693
Maximum Electrode Separation (m)	115	Voltage applied across current electrodes (V)	120
Number of stacks	2	Range of current output on point electrodes (mA)	61 to 1082
Electrical current window length	1s	Range of current output on long electrodes (mA)	1588 to 1866
Number of snapshots	780	Maximum current output difference on a single electrode (mA)	710
Time to acquire each snapshot (min)	14	Range of measured transfer resistance values (ohms)	0.0275 to 27.9

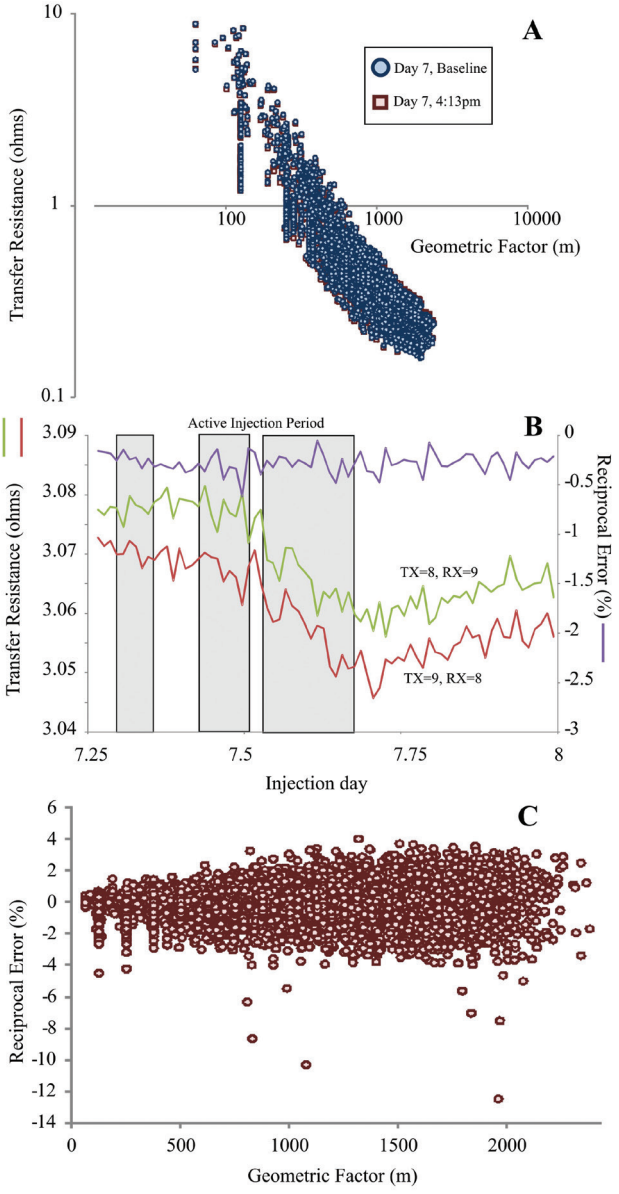

FIGURE 5

Plots demonstrating raw transfer resistance data from the resistivity acquisition system during the last day of monitoring. a) Transfer resistance versus geometric factor for the baseline and at the time of injection cessation on Day 7. b) Time series of transfer resistance for two reciprocal pairs with reciprocal error for Injection Day 7. c) Complete reciprocal error plot for baseline conditions of Injection Day 7.

monitoring system was set up to continuously record data during the injection campaign, including electrical current and voltage. Figure 6 displays the electrical current output on the borehole electrodes immediately to the north (borehole 111.1) of the injection well, at a lateral distance of 12.2 m. In our analysis, we assumed that a significant increase in the output current on an electrode equated to the reagent contacting that electrode, allow-

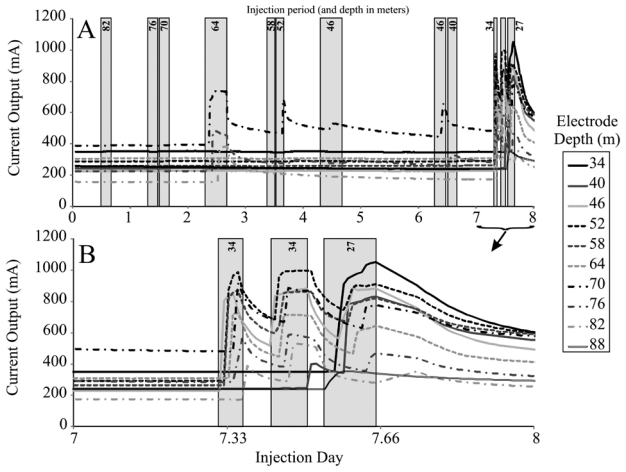

FIGURE 6

Electrical current output during reagent injection into a heap. The electrodes are located 12.2 m north of the injection well in borehole 111.1. a) Full series of current data over 8 days of injection. b) Last day of injection expanded to show details in the fluid arrival.

ing the position of the wetting front to be benchmarked in space and time. To improve clarity, only the electrodes registering an increase are displayed in Fig. 6; electrodes shallower than 34 m displayed a constant output current during the entire injection period. The constant output current recorded through the end of Day 1 indicates there was no reagent movement to the north during the first three injections. Although not shown here, the borehole immediately to the south (110.2) of the injection well indicated reagent arrivals during the injection at 70 m (bgs) as interpreted through output current increases on electrodes at depths of 70, 72 and 88 m (bgs). As the injection depth decreased, the wetting front shifted from arriving at the southern borehole to the northern borehole, with the injection at 64 m depth having arrivals on both the north and south boreholes.

Details of the Day 7 injection, at depths of 27 and 34 m (bgs), are displayed in Fig. 6(b). The shallow injections had a significant number of reagent arrivals on the electrodes of boreholes 111.1 and 111.2 (not shown in Fig. 6b), located at lateral distances of 12.2 and 24.4 m to the north of the injection well respectively. To summarize all of the arrivals over the 8 day period, we plotted the estimated maximum reagent propagation during each injection based on those electrodes that registered an increased output current (Fig. 7). The figure highlights the predominance of deeper injections registering reagent arrivals to the south, while shallower injections register arrivals to the north. The injection at depths of 40, 46 and 52 m (bgs) registered just one arrival, on the same electrode in borehole 111.1, while the injection at a depth of 58 m (bgs) did not register any arrivals. Interestingly, the injections at 27 and 34 m registered a significantly greater number of arrivals to the north compared to the previous injection depths. Overlain on the figure are the structural contacts within the heap presented in Fig. 4(b). The north-

erly dip of the structural contacts could help explain the reagent moving predominately to the north for shallow injections.

Apparent resistivity data for the electrodes in borehole 111.1, during current transmission on injection well 111, are displayed in Fig. 8. The conversion from measured voltage to apparent resistivity was accomplished using equation (5). The figure focuses on Day 7 of injections, as the greatest number of reagent arrivals were recorded for the injection on this day. The raw apparent resistivity data are presented as a function of depth and time (Fig. 8a). There is a strong near-linear trend of high- to low-apparent resistivity values moving upwards through the heap. Removing this trend by simple subtraction (Fig. 8b) produces apparent resistivity contours very similar to the forward modelling results presented earlier (Fig. 2c). The depths associated with each injection zone display an increase in apparent resistivity during the time of injection (shaded regions in Fig. 8). Overlain on Fig. 8(b) are dots representing the times that electrodes registered a reagent arrival, as indicated by an increase in output current. The timing indicates a progression of deeper electrodes wetting up in sequence as the reagent drains downward through the leach pad under the pull of gravity. In contrast, the voltage response only appears to be influenced by what is occurring in the injection zone. This could potentially be due to the way the heap is geomechanically altered during high-pressure injections. Seal, Rucker and Winterton (2012) summarized conditions during injection into an unconsolidated and non-cohesive rock pile, where it is likely that a fluid cavity is formed when the injection pressure exceeds the overburden pressures of heap material.

To verify claims that raw data of current and voltage can be used to make assessments of the subsurface during injection, the data were inverse modelled to produce volumetric images of the reagent's movement. Again, focusing on the last day of injection, 74 snapshots were extracted from the complete data set, starting at 6:38 am and finishing at 11:51 pm. The first three snapshots represented background conditions just prior to commencement of any injection. After removing noisy data based on reciprocal errors exceeding 5% and electrodes with poor ground coupling, a total of 125 out of the 144 point electrodes around injection well 111 were used in the inverse model. The number of non-reciprocal data points reduced from 7624 prior to data rejection to 6693 after rejection and the transfer resistance for each electrode pair comprised the average from the reciprocal measurement. Modelling was accomplished using RES3DINVx64 v.3.05.17, which incorporates both spatial and temporal smoothing constraints to allow all snapshots to be modelled together (Loke, Dahlin and Rucker 2013). Inversion parameters included: a homogeneous starting model obtained from the average of all apparent resistivity from the baseline data set, a smooth model spatial roughness filter (L_2 norm), a blocky temporal roughness filter (L_1 norm) and a uniform inverse model cell size of 3.8 m.

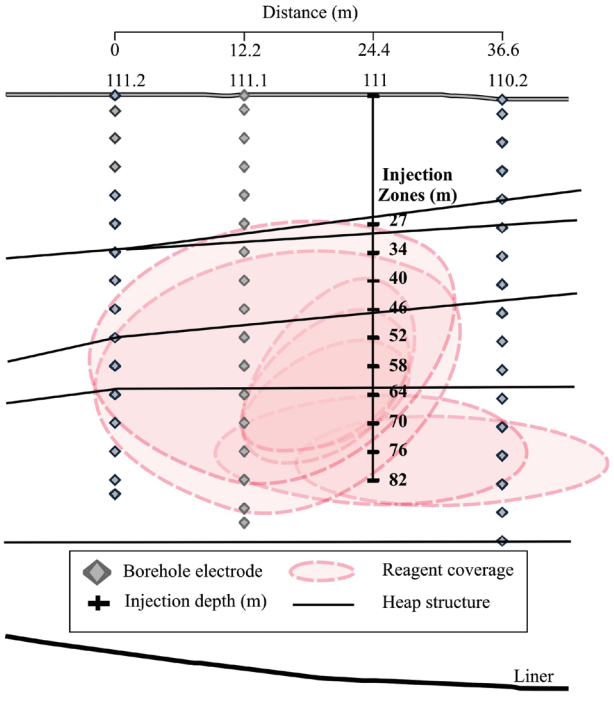

FIGURE 7

An interpretation of reagent coverage for each injection, determined by benchmarking arrivals as estimated from current output. Overlain on the figure are the structural contacts presented in Fig. 4(b).

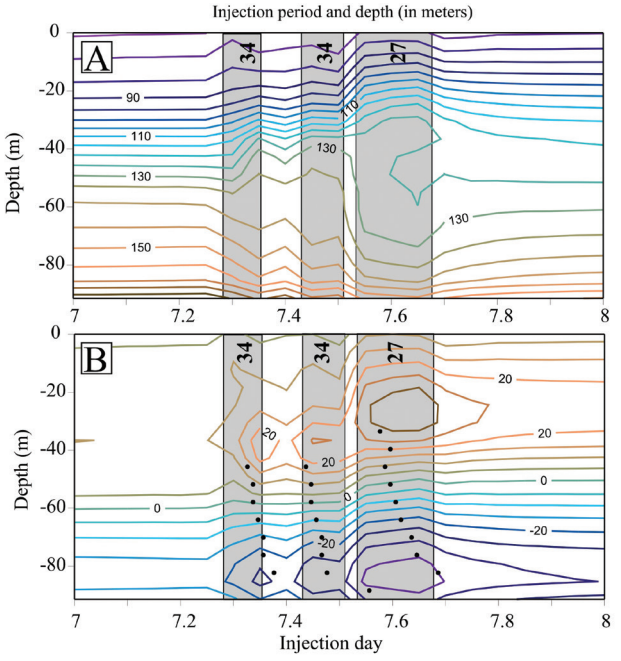

FIGURE 8

Apparent resistivity as a function of time observed on borehole 111.1 during the last day of monitoring. Injection timing and zones are identified by the grey bars. a) Raw apparent resistivity as measured from the resistivity acquisition system. b) Trend removed apparent resistivity. Reagent arrivals from interpretation of electrical current are overlain as dots.

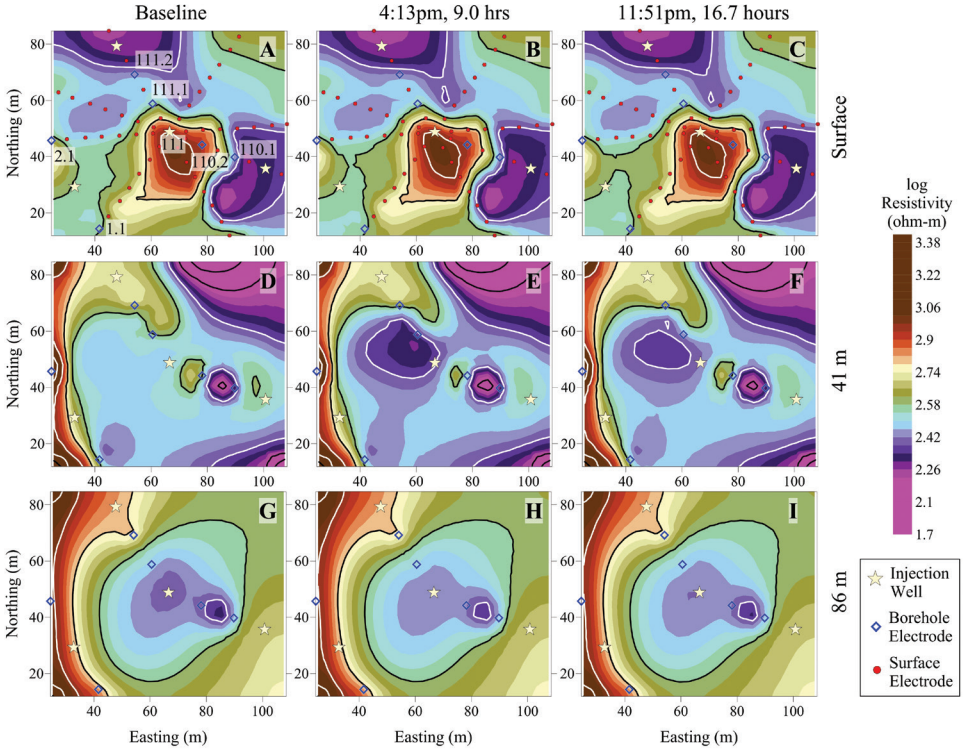

FIGURE 9
Horizontal slices through the inversion domain showing contoured values of electrical resistivity changing in time and space. Specific times and depths of the slices are presented above or to the right of the contoured sections.

The spatial and temporal roughness filters were chosen from a variety of tests conducted in Loke, Dahlin and Rucker (2013). The modelling took 3.6 days to complete five iterations on a 16-node platform, with a final misfit error between modelled and measured resistivity for all snapshots of 7.8%.

The first evaluation of the inversion results is in the form of simple image appraisal to evaluate coherency and adherence to our preconceived conceptual model. Figure 9 shows a series of horizontal slices through the domain with resistivity varying by nearly two orders of magnitude. The series of slices represent different times and different depths, with the first column showing the results of the initial snapshot at 6:38 am (Fig. 9a,d,g), the second column showing conditions at the end of the day's injection at 4:13 pm (Fig. 9b,e,h), and the last column showing the resistivity distribution for the last snapshot at 11:51 pm (Fig. 9c,f,i). The depths of the slices are at the surface, 41 m and 86 m (bgs) for rows 1–3 respectively. The surface shows low- and high- resistivity targets, with the highest resistivity near the centre of the injection area. As expected, the resistivity does not change appreciably during injection (Fig. 9a–c). The resistivity data at 41 m depth (Fig. 9d–f), just below the injection at 34 m, show the least variability in space but greatest variability across time. At the height of the injection (Fig. 9e), a large low-resistivity feature appears to the north-west of the injection well, which dissipates significantly at the end of monitoring (Fig. 9f). Near the bottom of the domain a low-resistivity feature is present near the well at the onset of injection (Fig. 9g), which disappears at the height of injection (Fig. 9h) and reappears again slightly at the end of monitoring (Fig. 9i). One hypothesis is that the solution from the previous day's injection is still present and draining. By the end of the injection, most of that reagent has drained below the model domain and by the end of the monitoring period a new volume of reagent has arrived.

Figure 10 shows the model resolution from the same series of slices as Fig. 9. The resolution is the highest at the surface due to the large number of surface electrodes, reducing by approximately two orders of magnitude at the bottom of the domain for a given location. The exception is at the borehole electrode locations, where the resolution stays particularly high throughout the inversion. Remarkably, the resolution does not change over time and it appears that the distribution of a conductive reagent has a negligible effect on the value. The high resolution near the borehole electrodes may explain the shape of some smaller targets observed in Fig. 9. For example, a conductive target is persistent between boreholes 110.1 and 110.2, with a shape and resistivity value that does not change to any significant degree during the course of injection.

To focus more on areas that change due to the reagent injection, Fig. 11 highlights results as a per cent change in conductivity (reciprocal of resistivity) from the baseline condition at 6:38 am. The figure emphasizes values of 3, 6 and 12 per cent change for both 3D rendered volumes and 2D vertical slices. There are six snapshots in the figure, with the first five snapshots at time intervals of 1.5–2 hours. Snapshot five represents the snapshot just as the injections ceased for the day and signifies the largest volume contribution by the reagent. It is the same time as pre-

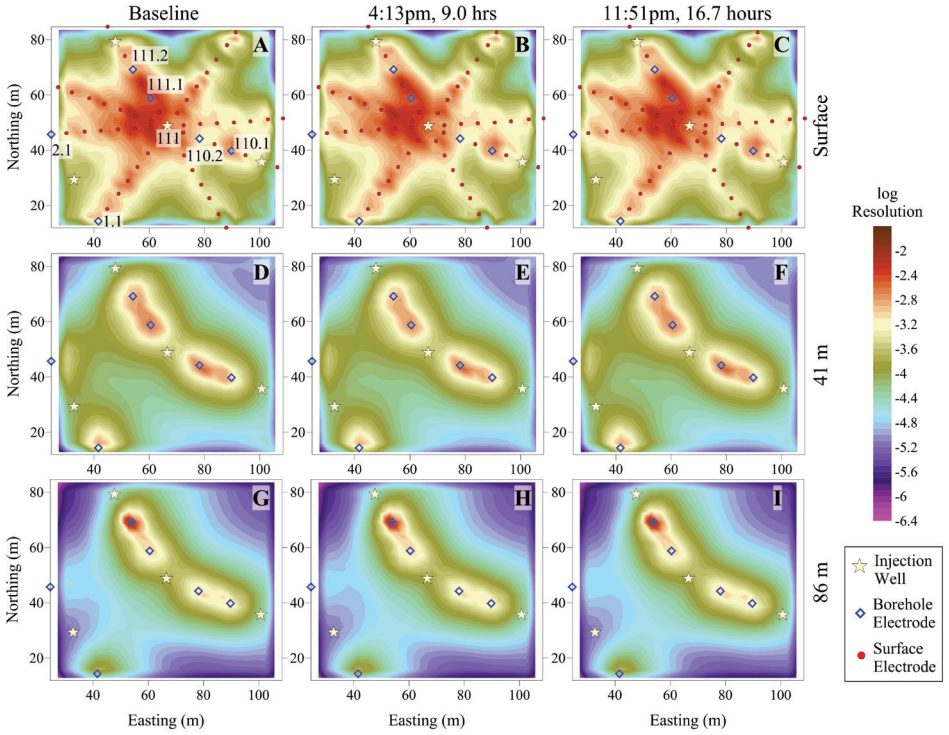

FIGURE 10
Horizontal slices through the inversion domain showing contoured values of model resolution. Specific times and depths of the slices are presented above or to the right of the contoured sections.

sented in Figs 9 and 10, subplots b, e and h of both figures. The last snapshot represents conditions at the end of the day to illustrate the slow drainage out of the domain and is the same time as presented in Figs 9 and 10, subplots c, f, and i. The vertical profiles accompanying the 3D rendered volumes are at a constant $x = 56$ m, which is between boreholes 111.1 and 111.2. Note the same reference coordinate system as those in Figs 4, 9 and 10.

During injections the inverted data indicate the reagent tending towards a westerly to north-westerly direction, in agreement with the raw output current data. However, there are key differences to note for the two data sets. While the output current shows the reagent front penetrating relatively deep into the heap during active injections, the inverse modelling results tend to be comparatively shallow. Two possible explanations for this include measurement errors leading to uncertainties in the inversion models and a lack of sufficient resolution with the pole-pole array to image through the conductive mass that is attributed to the injection. Measurement errors at the bottom of boreholes 111.1 and 111.2 may be forcing the area to become more resistive over time (Fig. 11). A negative conductivity change below the large conductive mass appears out of place. It is likely the inversion model could be rerun without the electrodes at the bottom of boreholes 111.1 and 111.2 to develop an improved representation of the reagent movement. Alternatively, it is known that the pole-pole array has the lowest resolving power, relative to the pole-dipole and dipole-dipole arrays. The pole-pole array was chosen for this work to take advantage of the benchmarking capabilities of the electrical current electrodes, low- transmitter power requirements, high received signal levels and to quickly conduct a full sweep of measurements in the shortest period of time. The low resolution of the model away from the borehole electrodes compared to regions immediately near the electrodes, as shown in Fig. 10, may be artificially introducing the resistive body below the conductive one as a means to compensate for the intensity of the reagent target. Clément *et al.* (2011) also described high- resistivity artefacts developing below conductive targets when using symmetric arrays. Furthermore, Robert *et al.* (2012) discussed a means to understanding noise in time-lapse inversion by comparing the results of two independent snapshots representing background conditions. We also conducted this assessment and found that the average background error was 0.0145% with a standard deviation of 0.045%. The background noise is quite low, likely as a direct result of the temporal smoothing constraint. Based on these statistics and the work by Robert *et al.* (2012), the per cent change in conductivity below approximately 0.15% could potentially be discarded as noise. Regardless, the inversion results display relatively good agreement with those obtained through electrical output current but the latter were assessed in real time. In addition, the propagation of the reagent interpreted from the output current includes fewer artefacts potentially making it a more reliable, albeit a lower resolved, tool for subsurface assessment.

CONCLUSIONS

An electrical resistivity monitoring survey was designed around an underground injection experiment, where a dilute sodium cyanide reagent was injected into an engineered rock pile (or heap) to increase the dissolution of metallic gold from low-grade

ore. The purpose of the monitoring was to track the movement of fluid from the injection well and observe the effectiveness of this new enhanced recovery technique to inundate regions that may be experiencing undesirable geochemical conditions, as well as provide a level of safety to ensure that the side slopes of the heap did not fail from over saturation. The survey design placed 150 electrodes around the injection well and included surface electrodes, borehole electrodes and six long electrodes. Using the pole-pole array and a high-capacity multi-channel resistivity acquisition system, a full sweep of measurements, where all possible electrode configurations were addressed including reciprocals, was acquired in 14 minutes. The resistivity monitoring system was run continuously during the experiment, through 10 individual injection zones over eight days.

A real-time assessment of the reagent's position was conducted by recording the time series of the electrical current from the borehole electrodes. It is well known that the contact resistance of a metallic electrode grounded to the earth will reduce substantially if water is added to its immediate surroundings. We took direct advantage of this fact by tracking a surrogate for the contact resistance, electrical current, as the approaching wetting front from the injection saturated the area near the borehole electrode. When conducted in this manner, the electrical resistivity technique is reduced from a large volumetric-based measurement to that of a point measurement in space, similar to other point-based hydrological sensors that measure pressure or moisture content. However, a stainless steel rod is significantly more robust and easier to install than most hydrological sensors. Furthermore, it can be used as a reliable mechanism to track the reagent's position without the intrusion of subjective regularization, data weighting and parametrization inherent in electrical resistivity tomography. It appears that the next step in deriving more accurate tomographic images could be to directly include the electrical current information as part of the objective function, similar to the work by Johnson *et al.* (2012) to include geostatistical constraints.

After demobilizing from the site, a significant effort was expended to produce 3D tomographic time-lapse images of the injection in order to both validate the electrical current data as well as fill in some of the information gaps where borehole electrodes were not present. The inversion used both spatial and temporal dampening constraints to produce images that were relatively smooth. In general, the information from the electrical current output and tomographic inversion matched; both methods showed a reagent plume moving towards the north-west. However, there are minor artefacts in the tomography that may be inhibiting a

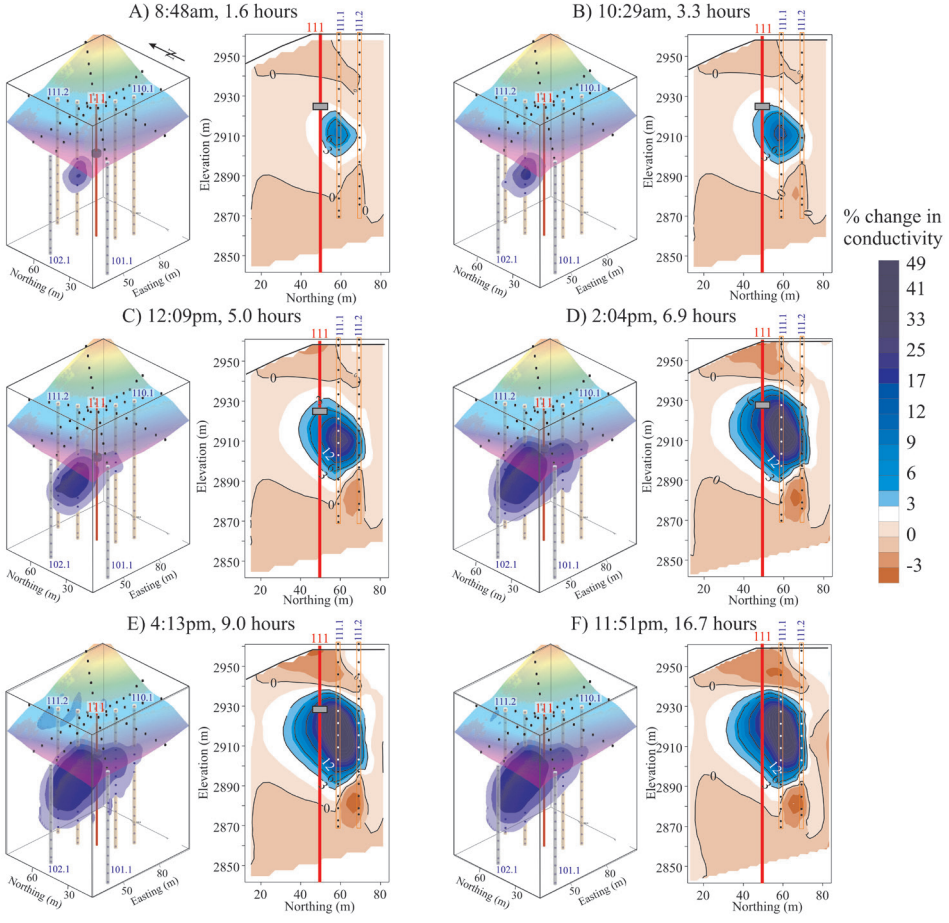

FIGURE 11
Inversion results from data extracted during the last day of injections at 34 and 27 m. The results are presented as per cent change from background conductivity (positive indicating an increase in conductivity) for both 3D rendered volumes and vertical slices at x = 56 m (between boreholes 111.1 and 111.2). The three transparent bodies of the 3D rendered plots represent 3, 6 and 12% change from background. Injection well 111 and monitoring boreholes are presented for reference (projected onto slice), along with the specific injection zone as a grey cylinder.

perfect match between the two data sets. Whereas the electrical current information showed the plume migrating deeply, the tomographic inversion had the plume held up in a shallower region of the heap. Investigating the model resolution, we discovered that the regions around boreholes had significantly higher values compared to regions far from the electrodes, potentially biasing the results. To combat this, a different array could be used where model resolution is more evenly distributed throughout the domain. Many have recognized that particular optimized arrays can produce better subsurface images (e.g., Stummer, Maurer and Green 2004; Loke, Wilkinson and Chambers 2010; Wilkinson *et al*. 2012), which could easily be employed here by transposing the pole-pole array to any desired four-pole array, as shown practically in Rucker (2012). When constrained by the electrical current information, it is anticipated that a new level of accuracy can be achieved in resistivity imaging.

REFERENCES

Alumbaugh D.L. and Newman G.A. 2000. Image appraisal for 2-D and 3-D electromagnetic inversion. *Geophysics* **65**, 1455–1467.

Calendine S., Rucker D.F., Fink J.B., Levitt M.T. and Schofield J. 2011. Automated leak detection of buried tanks using geophysical methods at the Hanford Nuclear Site. SAGEEP 2011. *Annual Meeting of the Environmental and Engineering Geophysical Society*, Charleston, SC. April 10–14, 2011.

Clément R., Descloitres M., Günther T., Oxarango L., Morra C., Laurent J.-P. and Gourc J.-P. 2011. Improvement of electrical resistivity tomography for leachate injection monitoring. *Waste Management* **30**, 452–464.

Constable S.C., Parker R.L. and Constable C.G. 1987. Occam's inversion: A practical algorithm for generating smooth models from electromagnetic sounding data. *Geophysics* **52**, 289–300.

Day-Lewis F.D., Singha K. and Binley A.M. 2005. Applying petrophysical models to radar travel time and electrical resistivity tomograms: Resolution-dependent limitations. *Journal of Geophysical Research* **110**, B08206.

deGroot-Hedlin C. and Constable S.C. 1990. Occam's inversion to generate smooth, two-dimensional models from magnetotelluric data. *Geophysics* **55**, 1613–1624.

Doetsch J., Linde N., Vogt T., Binley A. and Green A.G. 2012. Imaging and quantifying salt-tracer transport in a riparian groundwater system by means of 3D ERT monitoring. *Geophysics* **77**, B207–218.

Farquharson C.G. 2008. Constructing piecewise-constant models in multidimensional minimum-structure inversions. *Geophysics* **73**, K1–K9.

Farquharson C.G. and Oldenburg D.W. 1998. Nonlinear inversion using general measures of data misfit and model structure. *Geophysical Journal International* **134**, 213–227.

Friedel S. 2003. Resolution, stability and efficiency of resistivity tomography estimated from a generalized inverse approach. *Geophysical Journal International* **153**, 305–316.

Ha C., Kim N., Park H., Kwon S.Y., Lee H.S., Hong U.J. *et al*. 2011. Natural gradient drift tests for assessing the feasibility of in situ aerobic cometabolism of trichloroethylene and evaluating the microbial community change. *Water, Air and Soil Pollution* **219**, 353–364.

Johnston R.H., Trofimenkoff F.N. and Hasslett J.W. 1987. Resistivity response of a homogeneous earth with a finite-length contained vertical conductor. *IEEE Transactions on Geoscience and Remote Sensing* **GE-25**(4), 414–421.

Johnson T.C., Versteeg R.J., Rockhold M., Slater L.D., Ntarlagiannis D., Greenwood W.J. *et al.* 2012. Characterization of a contaminated well field using 3D electrical resistivity tomography implemented with geostatistical, discontinuous boundary, and known conductivity constraints. *Geophysics* **77**, EN85–EN96.

Johnson T.C., Versteeg R.J., Ward A., Day-Lewis F.D. and Revil A. 2010. Improved hydrogeophysical characterization and monitoring through parallel modeling and inversion of time-domain resistivity and induced-polarization data. *Geophysics* **74**, WA27–WA41.

Kim J.H., Yi M.J., Park S.G. and Kim J.G. 2009. 4D inversion of DC resistivity monitoring data acquired over a dynamically changing earth model. *Journal of Applied Geophysics* **68**, 522–532.

LaBrecque D.J., Heath G., Sharpe R. and Versteeg R. 2004. Autonomous monitoring of fluid movement using 3-D electrical resistivity tomography. *Journal of Environmental and Engineering Geophysics* **9**, 167–176.

LaBrecque D.J., Miletto M., Daily W., Ramirez A. and Owen E. 1996. The effects of noise on Occam's inversion of resistivity tomography data. *Geophysics* **61**, 538–548.

Lee M., Kim J. and Kim I. 2011. In-situ biosurfactant flushing, coupled with a highly pressurized air injection, to remediate the bunker oil contaminated site. *Geosciences Journal* **15**, 313–321

Lile O.B., Morris M. and Rønning J.S. 1997. Estimating groundwater flow velocity from changes in contact resistance during a saltwater tracer experiment. *Journal of Applied Geophysics* **38**, 105–114.

Loke M.H., Acworth I. and Dahlin T. 2003. A comparison of smooth and blocky inversion methods in 2D electrical imaging surveys. *Exploration Geophysics* **34**, 182–187.

Loke M.H. and Barker R.D. 1996. Practical techniques for 3D resistivity surveys and data inversion. *Geophysical Prospecting* **44**, 499–523.

Loke M.H., Dahlin T. and Rucker D.F. 2013. Smoothness-constrained time-lapse inversion of data from 3-D resistivity surveys. *Near Surface Geophysics* (in press).

Loke M.H., Wilkinson P.B. and Chambers J.E. 2010. Parallel computation of optimized arrays for 2-D electrical imaging surveys. *Geophysical Journal International* **183**, 1302–1315.

Lwambiyi M., Maweja K., Kongolo K., Lwambiyi N.M. and Diyambi M. 2009. Investigation into the heap leaching of copper ore from the Disele deposit. *Hydrometallurgy* **98**, 177–180.

Navarro A. and Martínez F. 2010. The use of soil-flushing to remediate metal contamination in a smelting slag dumping area: Column and pilot-scale experiments. *Engineering Geology* **115**, 16–27.

Nguyen F., Kemna A., Antonsson A., Engesgaard P., Kuras O., Ogilvy R. *et al*. 2009. Characterization of seawater intrusion using 2D electrical imaging. *Near Surface Geophysics* **7**, 377–390.

Oldenburg D.W. and Li Y. 1999. Estimating depth of investigation in DC resistivity and IP surveys. *Geophysics* **64**, 403–416.

Pidlisecky A., Cockett and Knight R. 2012. The Development of Electrical Conductivity Probes for Studying Vadose Zone Processes: Advances in Data Acquisition and Analysis. *Vadose Zone Journal* (in review).

Robert T., Caterina D., Deceuster J., Kaufmann O. and Nguyen F. 2012. A salt tracer test monitored with surface ERT to detect preferential flow and transport paths in fractured/karstified limestones. *Geophysics* **77**, B55–B67.

Rucker D.F. 2009. A coupled electrical resistivity-infiltration model for wetting front evaluation. *Vadose Zone Journal* **8**(2), 383–388.

Rucker D.F. 2012. Enhanced resolution for long electrode ERT. *Geophysical Journal International* **191**, 101–111.

Rucker D.F., Crook N., Glaser D.R. and Loke M.H. 2012. Pilot-Scale Field Validation of the Long Electrode Electrical Resistivity Tomography Method. *Geophysical Prospecting* **60**(6), 1150–1166.

Rucker D.F., Fink J.B. and Loke M.H. 2011. Environmental monitoring of leaks using time lapse long electrode electrical resistivity. *Journal of Applied Geophysics* **74**, 242–254.

Rücker C. and Günther T. 2011. The simulation of finite ERT electrodes using the complete electrode Model. *Geophysics* **76**, F227–F238.

Rucker D.F., Loke M.H., Noonan G.E. and Levitt M.T. 2010. Electrical resistivity characterization of an industrial site using long electrodes. *Geophysics* **75**, WA95–WA104.

Rucker D.F., McNeill M., Schindler A. and Noonan G.E. 2009a. Monitoring of a secondary recovery application of leachate injection into a heap. *Hydrometallurgy* **99**, 238–248.

Rucker D.F., Schindler A., Levitt M.T. and Glaser D.R. 2009b. Three-dimensional electrical resistivity imaging of a gold heap. *Hydrometallurgy* **98**, 267–275.

Seal T., Rucker D.F. and Winterton J. 2012. Enhancing gold recovery using Hydro-Jex© at Cripple Creek and Victor Gold Mine Co. In: *Separation Technologies for Minerals, Coal & Earth Resources*, (eds C.A. Young and G.H. Luttrell). Society for Mining, Metallurgy, and Exploration, Denver.

Stummer P., Maurer H. and Green A. 2004. Experimental design: Electrical resistivity data sets that provide optimum subsurface information. *Geophysics* **69**,120–129.

Svab M., Kubal M., Müllerova M. and Raschman R. 2009. Soil flushing by surfactant solution: Pilot-scale demonstration of complete technology. *Journal of Hazardous Materials* **163**, 410–417.

Telford W., Geldart L. and Sheriff R. 1990. *Applied Geophysics*. Cambridge University Press, Cambridge.

Warrick A.W. and Rojano A. 1999. Effects of source cavity shape on steady, three-dimensional flow of soil gases. *Water Resources Research* **35**, 1425–1433.

Wilkinson P.B., Loke M.H., Meldrum P.I., Chambers J.E., Kuras O., Gunn D.A. *et al.* 2012. Practical aspects of applied optimized survey design for electrical resistivity tomography. *Geophysical Journal International* **189**, 428–440.

Wilkinson P.B., Meldrum P.I., Kuras O., Chambers J.E., Holyoake S.J. and Ogilvy R.D. 2010. High-resolution electrical resistivity tomography monitoring of a tracer test in a confined aquifer. *Journal of Applied Geophysics* **70**, 268–276.